

Breaking size segregation waves and particle recirculation in granular avalanches

A. R. THORNTON AND J. M. N. T. GRAY

School of Mathematics and Manchester Centre for Nonlinear Dynamics, University of Manchester,
Oxford Road, Manchester, M13 9PL, UK

(Received 27 April 2007 and in revised form 5 October 2007)

Particle-size segregation is a common feature of dense gravity-driven granular free-surface flows, where sliding and frictional grain–grain interactions dominate. Provided that the diameter ratio of the particles is not too large, the grains segregate by a process called kinetic sieving, which, on average, causes the large particles to rise to the surface and the small grains to sink to the base of the avalanche. When the flowing layer is brought to rest this stratification is often preserved in the deposit and is known by geologists as inverse grading. Idealized experiments with bi-disperse mixtures of differently sized grains have shown that inverse grading can be extremely sharp on rough beds at low inclination angles, and may be modelled as a concentration jump or shock. Several authors have developed hyperbolic conservation laws for segregation that naturally lead to a perfectly inversely graded state, with a pure phase of coarse particles separated from a pure phase of fines below, by a sharp concentration jump. A generic feature of these models is that monotonically decreasing sections of this concentration shock steepen and eventually break when the layer is sheared. In this paper, we investigate the structure of the subsequent breaking, which is important for large-particle recirculation at the bouldery margins of debris flows and for fingering instabilities of dry granular flows. We develop an exact quasi-steady travelling wave solution for the structure of the breaking/recirculation zone, which consists of two shocks and two expansion fans that are arranged in a ‘lens’-like structure. A high-resolution shock-capturing numerical scheme is used to investigate the temporal evolution of a linearly decreasing shock towards a steady-state lens, as well as the interaction of two recirculation zones that travel at different speeds and eventually coalesce to form a single zone. Movies are available with the online version of the paper.

1. Introduction

There are many mechanisms for segregation of dissimilar grains in granular flows (e.g. Bridgewater 1976; Cooke, Stephens & Bridgewater 1976; Drahun & Bridgwater 1983; Aranson & Tsimring 2006), but *kinetic sieving* (Middleton 1970) is the mechanism that usually dominates in high-solids-fraction ($0.49 < \nu < 0.64$) gravity-driven avalanches and chute flows, in which sliding and rolling contacts prevail over collisional ones. As a granular avalanche flows down a rough slope it is sheared through its depth and dilates sufficiently for the particles to percolate relative to one another. Kinetic sieving describes the gravity-driven process in which small particles tend to fall into gaps that open up beneath them, because they are statistically more likely to fit into the available space than the large ones. The

avalanche acts as a *random fluctuating sieve* (Savage & Lun 1988) that allows small particles to preferentially percolate downwards and force imbalances generate a non-size-preferential return flow, termed *squeeze expulsion* (Savage & Lun 1988), that keeps the solids volume fraction approximately uniform. The net effect is for small particles to percolate downwards and the coarse ones to rise up. This process is so efficient in slow dry frictional flows that sufficiently far downstream zones with 100 % fines and 100 % coarse particles are formed that are separated by a sharp jump in species concentration (Savage & Lun 1988; Vallance & Savage 2000). In more rapid energetic flows, on steeper slopes, kinetic sieving competes with diffusive remixing and the shocks are smoothed out to form ‘S’-shaped steady-state concentration profiles through the avalanche depth. The tendency for the concentration of larger particles to increase towards the surface of the flow is known as inverse or reverse grading (e.g. Bagnold 1954; Middleton 1970; Middleton & Hampton 1976; Sallenger 1979; Naylor 1980) and is seen in sedimentary deposits from many geophysical mass flows, including debris flows, the dense basal layers of pyroclastic flows and turbidity currents, as well as deposits from avalanches of sand, rock and snow.

Savage & Lun (1988) developed the first continuum model of kinetic sieving for a simplified bi-disperse mixture of large and small grains. The particles were assumed to lie in a series of layers parallel to the base that sheared over one another, and a statistical mechanical description of the voids was used to model the random fluctuating sieve and squeeze expulsion mechanisms. This allowed them to derive expressions for the constituent percolation velocities normal to the chute, and a steady-state segregation equation for the number density ratio η of small to large grains. In the small-particle dilute limit Savage & Lun (1988) used the method of characteristics and global mass balance to derive an approximate solution for the spatial development of the particle-size distribution from a homogeneous inflow. For a steady uniform shear flow they showed that the solution had three constant-concentration regions that were separated by sharp concentration jumps or shocks. Two of the shocks emanated from the surface and base of the inflow and propagated inwards, eventually intersecting to form a third, slope-parallel, shock between pure phases of large and small particles. This was in qualitative agreement with observations that they made through the transparent sidewall of their chute, a picture of which is reproduced in Thornton, Gray & Hogg (2006). Savage & Lun (1988) and Vallance & Savage (2000) used a movable hopper and a series of splitter plates to collect samples from various positions in the flow. This allowed them to build up detailed data sets on the steady-state particle-size distribution as it evolved with downstream distance. Although this method was not accurate enough to explicitly resolve the concentration shocks, Savage & Lun (1988) and Vallance & Savage (2000) used a binning procedure to show that their approximate solutions were consistent with their experimentally sampled data.

1.1. The hyperbolic segregation equation

The leading-order structure of Savage & Lun’s (1988) segregation flux has also been found independently by other authors. Dolgunin & Ukolov (1995) argued that particle segregation must shut off when either coarse or fine grains are in a pure phase, and inferred from this that, to leading order, the flux must be proportional to the volume fraction of fines multiplied by the volume fraction of coarse grains. More recently Gray & Thornton (2005) and Thornton *et al.* (2006) have used two- and three-constituent mixture theory to derive a non-dimensional scalar hyperbolic

conservation law for the small-particle concentration $\phi(x, y, z, t) \in [0, 1]$

$$\frac{\partial \phi}{\partial t} + \frac{\partial}{\partial x}(\phi u) + \frac{\partial}{\partial y}(\phi v) + \frac{\partial}{\partial z}(\phi w) - \frac{\partial}{\partial z}(S_r \phi(1 - \phi)) = 0, \quad (1.1)$$

where the non-dimensional bulk velocity components (u, v, w) lie in the downslope, cross-slope and normal directions, (x, y, z) , respectively, and S_r is the non-dimensional segregation number. The large particles occupy a volume fraction $1 - \phi$ and the segregation flux $\mathcal{F} = -S_r \phi(1 - \phi)$. This is the same as the flux in Savage & Lun's (1988) dilute limit (although it was formulated in terms of the number density ratio) and which was postulated directly by Dolgunin & Ukolov (1995). The strong links between the theories imply that the segregation model (1.1) has already been compared to the results of an extensive series of laboratory experiments by Savage & Lun (1988), Dolgunin & Ukolov (1995) and Vallance & Savage (2000).

Equation (1.1) is the simplest possible segregation equation and makes several important assumptions and simplifications. The main hypotheses in Gray & Thornton (2005) and Thornton *et al.*'s (2006) derivation are: (i) the mixture is bi-disperse, (ii) the large and small grains have the same bulk density, (iii) the bulk flow is incompressible, (iv) the normal pressure is lithostatic, (v) the bed load is shared asymmetrically between the large and small particles, with the large particles carrying proportionally more of the load, (vi) momentum is transferred between particles at a velocity-dependent rate (by analogy with Darcy's Law), (vii) normal accelerations can be neglected, (viii) squeeze expulsion maintains a constant solids volume fraction, and (ix) diffusive remixing is negligible. With these assumptions, the normal components of the constituent momentum balances yield simple expressions for the normal percolation velocities of the large and small particles. These are based on a dominant balance between the rate-dependent drag and the deviation of the constituent pressure gradients away from lithostatic. The deviations arise because the small particles support less of the overburden pressure as they percolate down through the gaps, and the large particles must therefore support correspondingly more of the load, as they are driven up by squeeze expulsion.

Substituting the small-particle percolation velocity into the small-particle mass balance equation yields the segregation equation (1.1). All the physical parameters are encapsulated into a single non-dimensional segregation number,

$$S_r = \frac{LQ}{HU}, \quad (1.2)$$

which is the ratio of a typical downstream transport time scale, L/U , to a typical time scale for segregation, H/Q , where U is the magnitude of the downstream velocity, Q is the magnitude of the segregation velocity, and H and L are typical thicknesses and lengths of the avalanche. Slower downstream transport velocities, or faster normal segregation velocities, increase S_r and the material will therefore segregate in a shorter distance. The most general form of Q is given by the three-constituent theory of Thornton *et al.* (2006), which explicitly incorporates a passive fluid in the pore space between the large and small particles. In this theory $Q = (B/c)\hat{\rho}g \cos \zeta$, where B is the non-dimensional magnitude of the pressure perturbations, c is the inter-particle drag coefficient, ζ is the inclination angle of the chute and $\hat{\rho} = (\rho^{g*} - \rho^{a*})/\rho^{g*}$ is the relative density difference of the grains, ρ^{g*} , and the interstitial fluid, ρ^{a*} . Gray & Thornton (2005) used a simplified two-constituent approach to derive (1.1), which assumes that the interstitial pore space is incorporated into the bulk density of the large and small particles. This yields a similar Q , but with $\hat{\rho} = 1$. While both of these theories provide

a natural way of introducing the gravity dependence of the kinetic sieving process into the theory, they do not provide detailed dependences of S_r on the local shear rate, the particle-size ratio, the solids fraction or the local pressure. Investigations are currently underway to empirically determine these functional dependences through experiments and discrete element simulations.

The concentration shocks inherent in hyperbolic segregation models are an idealization of the sharp concentration transitions that occur in experiments and the real world. However, the simplicity of the hyperbolic approach lays bare the underlying structure in the low diffusive-remixing limit of more complex parabolic models (Dolgunin & Ukolov 1995; Dolgunin, Kudy & Ukolov 1998; Khakhar, McCarthy & Ottino 1997; Khakhar, Orpe & Hajra 2002; Gray & Chugunov 2006) in which smoothing is introduced by inter-particle diffusion. These models yield steady states with 'S'-shaped concentration profiles, rather than a sharp shock, and are in close agreement (Khakhar *et al.* 1997; Gray & Chugunov 2006) with the results of three-dimensional discrete-element simulations for both density and size segregation (Khakhar, McCarthy & Ottino 1999) in high-solids-fraction flows. This, together with the experimental results of Savage & Lun (1988), Dolgunin & Ukolov (1995) and Vallance & Savage (2000), provide strong evidence for a theory with the segregation flux used in the current models. There are, however, important effects that are not included, such as (i) feedback between the local particle concentration and the bulk flow, (ii) variations in the solids volume fraction, (iii) spatial variation of S_r and (iv) deformation of the free surface, that are all in need of further investigation.

1.2. Breaking sharply segregated inversely graded concentration shocks

In the hyperbolic segregation theory (1.1) shock waves develop naturally and practical problems may be solved by the method of characteristics (e.g. Bressan 2000). Gray & Thornton (2005) formulated the associated concentration jump condition at a surface of discontinuity, and used it to construct exact solutions to Savage & Lun's (1988) homogeneous inflow problem for arbitrary shear profiles. Thornton *et al.* (2006) developed an exact steady-state solution for a normally graded inflow, i.e. with all the small particles above the coarse grains. This configuration is unstable and immediately generates a centred expansion fan at the inflow, but sufficiently far downstream the grains separate out into sharply segregated inversely graded layers once again. Gray, Shearer & Thornton (2006) and Shearer, Gray & Thornton (2008) have gone on to construct fully time-dependent exact solutions to the homogeneous and normally graded inflow problems for different initial conditions, which exhibit fully dynamic propagating shocks and expansion fans.

The two problems discussed by Gray *et al.* (2006) are particularly interesting, because they generate a propagating inversely graded concentration shock that breaks in finite time. For this situation to develop a section of the shock must decrease in height with increasing downstream distance, as shown schematically in figure 1(a). In a shear flow, in which the upper layers move faster than the lower ones, the concentration shock will steepen, break and become triple-valued in the absence of segregation (figure 1b). When $S_r \neq 0$ the overhanging section of the shock is dynamically unstable and violates the Lax entropy condition (Shearer *et al.* 2008), i.e. there is an unstable stratification with small particles above large particles. There must therefore be a readjustment due to particle-size segregation, which seeks to establish a dynamically stable configuration. This paper is concerned with the subsequent structure of the breaking wave solution.

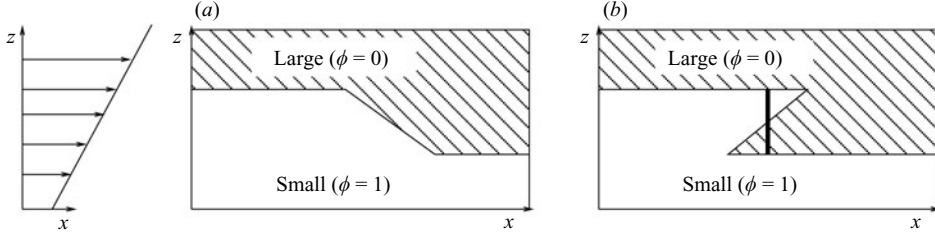


FIGURE 1. A schematic diagram showing how a monotonically decreasing section of an inversely graded sharply segregated concentration shock (a), steepens and eventually becomes triple-valued in the absence of segregation (b). When segregation does take place the overhanging section of the shock is dynamically unstable and the wave breaks.

Breaking segregation waves are fundamental features of all hyperbolic segregation models and their understanding also sheds light on parabolic solutions in the low diffusive-remixing limit. They are in many ways analogous to classical wave breaking phenomena in gas dynamics (Lighthill 1978) and fluids (Stoker 1957), but instead of a simple shock-fitting procedure, we shall show that a much more complicated structure evolves, consisting of two shocks and two expansion fans that are arranged in a propagating ‘lens’-like structure. We shall also show that these ‘lenses’ allow the large and the small particles to be recirculated as they are advected downstream. Recirculation zones have been observed in small-scale bi-disperse dry granular fingering experiments (Pouliquen, Delour & Savage 1997; Pouliquen & Vallance 1999) in which the larger particles are rougher than the fine grains. As the material avalanches downslope, large particles rise towards the faster moving surface layers and are transported to the flow front. If the roughness contrast, flow composition and slope inclination angle are correctly chosen, the large rough particles stop and are over-run by the bulk avalanche. Pouliquen *et al.* (1997) used tracers to show that these particles then re-emerged at the free surface again, some way upstream of the propagating front, and inferred from this that there was a recirculation loop in which the large particles rose by particle-size segregation. Similar processes take place at the bouldery margins of debris and pyroclastic flows (Pierson 1986; Vallance & Savage 2000; Vallance 2000; Iverson & Vallance 2001; Iverson 2005), and the enhanced resistance at these fronts can lead to the spontaneous generation of coarse-grained lateral levees, which channelize the flow and enhance run-out. There are therefore many important potential applications of this theory.

2. Travelling wave solution

An exact travelling wave solution for the breaking wave will now be constructed for a non-dimensional bulk flow of unit height and with bulk velocity

$$u = u(z), \quad v = 0, \quad w = 0, \quad \forall x, \quad \text{in } 0 \leq z \leq 1. \quad (2.1)$$

On first inspection, the quasi-steady structure is by no means obvious, but, for constant segregation number S_r , the solution consists of two shocks and two expansion fans that form a ‘lens’, which propagates downstream with velocity u_{lens} as shown schematically in figure 2. Upstream of the breaking wave the concentration shock is assumed to be of constant height $z = H_{\text{up}}$, and downstream of it the shock lies at $z = H_{\text{down}}$, where H_{up} is necessarily greater than H_{down} for the breaking wave to form. As these sections of the shock are of constant height and are parallel to the velocity shear, they remain

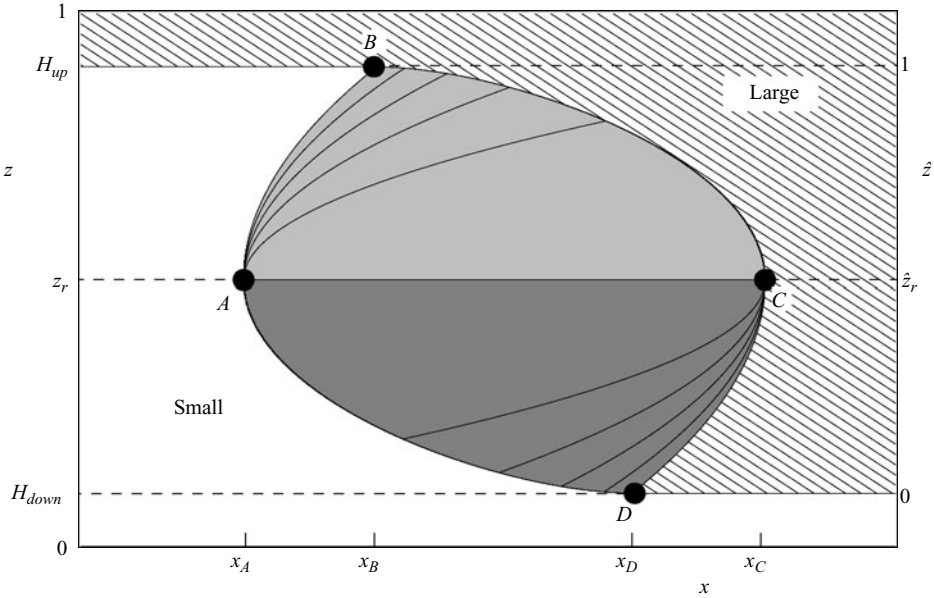


FIGURE 2. Schematic diagram of a breaking segregation wave showing the quasi-steady ‘lens’-like structure (grey shaded region), which propagates downslope at speed u_{lens} . There is a sharply segregated inversely graded shock at height $z = H_{up}$, upstream of the lens, and a further section at height $z = H_{down}$ downstream of it. The line $z = z_r$ marks the height at which the flow speed is equal to the lens speed. Above this line the net flow is to the right, and small particles are sheared towards the lens, while below $z = z_r$ the flow is to the left and large particles are dragged back into it. The lens itself consists of two expansion fans, centred at (x_A, z_r) and (x_C, z_r) , and two concentration shocks initiated from (x_B, H_{up}) and (x_D, H_{down}) that meet the fans to close the solution. The thin black lines inside the shaded regions indicate the characteristics within the expansion fans. The upper expansion initiated from point A has a lower concentration than the lower fan that is initiated at point C. It is therefore shaded as a lighter shade of grey. Non-dimensional heights are indicated along the left-hand axis and the transformed stretched heights are shown along the right-hand side.

at a constant height at all times. The mean velocity of the flow between these two heights defines the lens propagation speed

$$u_{lens} = \frac{1}{H_{up} - H_{down}} \int_{H_{down}}^{H_{up}} u(z) dz. \quad (2.2)$$

The solution assumes that the downstream velocity component u is strictly increasing with increasing height z . It follows that the lens propagates downstream faster than the basal slip velocity u_b , but slower than the free-surface velocity u_s . At height $z = z_r$ the bulk flow velocity is equal to the lens speed u_{lens} and it follows that above $z = z_r$ the flow is faster than the breaking wave and small particles are supplied from the left towards the lens. Below $z = z_r$, the flow is slower, and large particles are dragged back towards the lens from the right. This change in relative flow direction is crucial, and both expansion fans are initiated from $z = z_r$ at downstream positions x_A and x_C as shown in figure 2. The lead characteristics propagate away from this line and eventually intersect with the constant-height sections of the concentration shock at x_B and x_D , where two shocks are initiated that close the lens structure.

Having postulated the structure of the solution we now solve the segregation equation in a frame moving downslope with speed u_{lens} . Introducing the change of

variables

$$\hat{t} = \frac{S_r}{H_{up} - H_{down}} t, \quad \hat{x} = \frac{S_r}{H_{up} - H_{down}} (x - u_{lens} t), \quad \hat{z} = \frac{z - H_{down}}{H_{up} - H_{down}}, \quad (2.3)$$

the segregation equation (1.1) transforms to the convenient parameter-independent form

$$\frac{\partial \phi}{\partial \hat{t}} + \frac{\partial}{\partial \hat{x}}(\phi \hat{u}) - \frac{\partial}{\partial \hat{z}}(\phi(1 - \phi)) = 0, \quad (2.4)$$

where the relative downstream velocity \hat{u} is defined as

$$\hat{u} = u - u_{lens}. \quad (2.5)$$

The transformation (2.3) stretches the vertical coordinate, so that the top of the lens lies at $\hat{z} = 1$ and the bottom lies at $\hat{z} = 0$ as shown in figure 2. The line $\hat{z} = \hat{z}_r$ is the height where there is no mean flow, and $\hat{u} = 0$ relative to the propagating lens. Material below \hat{z}_r is therefore swept to the left, while material above \hat{z}_r is swept to the right.

For steady-travelling waves, equation (2.4) reduces to the quasi-linear equation

$$\hat{u} \frac{\partial \phi}{\partial \hat{x}} - \frac{\partial}{\partial \hat{z}}(\phi(1 - \phi)) = 0, \quad (2.6)$$

which can be solved by the method of characteristics. The concentration ϕ is equal to a constant ϕ_λ on the characteristic curve given by

$$\hat{u}(\hat{z}) \frac{d\hat{z}}{d\hat{x}} = (2\phi_\lambda - 1). \quad (2.7)$$

This can be integrated for arbitrary velocity fields by defining a depth-integrated flux coordinate (Gray & Thornton 2005)

$$\psi(\hat{z}) = \int_0^{\hat{z}} \hat{u}(\hat{z}') d\hat{z}', \quad (2.8)$$

which reduces equation (2.7) to a very simple linear ordinary differential equation

$$\frac{\partial \psi}{\partial \hat{x}} = 2\phi_\lambda - 1. \quad (2.9)$$

Integrating (2.9) subject to the condition that the characteristic starts at $(\hat{x}_\lambda, \psi_\lambda)$ implies

$$\psi = \psi_\lambda + (2\phi_\lambda - 1)(\hat{x} - \hat{x}_\lambda). \quad (2.10)$$

The characteristic curves are therefore all straight lines in the transformed mapped coordinate system as illustrated in figure 3. The mapping (2.8) has the property that $\psi = 0$ at $\hat{z} = 0$ and 1, and the coordinate has a minimum at $\psi = \psi_r < 0$ at $\hat{z} = \hat{z}_r$. The mapped domain is therefore essentially composed of two domains that are patched together along the dash-dot centreline in figure 3. In the upper domain ψ ranges from ψ_r to 0 and the bulk flow and the time-like direction are to the right, while in the lower domain, ψ ranges from 0 to ψ_r and the bulk flow and time-like directions are to the left. A small-particle characteristic ($\phi_\lambda = 1$), that starts to the left of the lens at the lower boundary $\hat{z} = 0$, is therefore swept first to the left in the lower domain and then to the right in the upper domain as shown in figure 3. Large-particle characteristics, $\phi_\lambda = 0$, start to the right of the lens at the upper boundary and are initially swept to the right before being swept to the left.

We may now solve for the structure of the lens. We start by placing a centred expansion fan at an arbitrary downslope position \hat{x}_A and at height $\psi = \psi_r$. Within

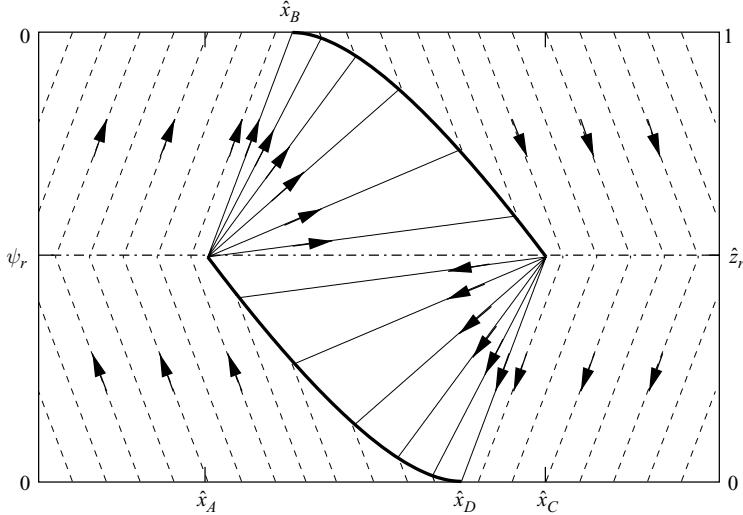


FIGURE 3. A diagram showing the characteristic curves in transformed coordinates (\hat{x}, ψ) . The dot-dash line at $\psi = \psi_r$ divides the coordinates into two domains. In the upper domain the bulk flow and the time-like direction are to the right, and ψ runs from ψ_r to 0, while in the lower domain the bulk flow and time-like direction are to the left, and ψ runs from 0 to ψ_r . The arrowed dashed lines indicate the time-like direction of the characteristic curves for pure phases of large and small particles, which emanate from the upper and lower boundaries, respectively. The solid arrowed lines show the centred expansion fans at \hat{x}_A and \hat{x}_C , and the thick black lines are the concentration shocks that emanate from \hat{x}_B and \hat{x}_D . The characteristics and shocks have 180° rotational symmetry about the centre of the lens.

the expansion the concentration is given by

$$\phi = \frac{1}{2} \left[1 + \frac{\psi - \psi_r}{\hat{x} - \hat{x}_A} \right]. \quad (2.11)$$

The characteristic curves emanating from the expansion only propagate upwards into the region that is flowing downslope relative to the lens. It follows that the concentration ϕ lies in the range $[1/2, 1]$. The $\phi = 1$ characteristic marks the boundary of the lens and the region of small particles that are being transported from the left towards it, and is given by the curve

$$\psi = \psi_r + \hat{x} - \hat{x}_A. \quad (2.12)$$

This reaches the upstream section of the concentration shock ($z = H_{up}$) at transformed mapped height $\psi = 0$ and position

$$\hat{x}_B = \hat{x}_A - \psi_r. \quad (2.13)$$

At this point there are no more small particles transported from the left, nor are there any supplied from above, so the large particles that are being transported upwards within the breaking wave separate out into a pure phase across a shock that is initiated at $\hat{x} = \hat{x}_B$, $\psi = 0$. Following Gray & Thornton (2005) the concentration jump condition across a steady propagating shock is

$$\left[\hat{u} \phi \frac{d\hat{z}}{d\hat{x}} + \phi(1 - \phi) \right] = 0, \quad (2.14)$$

where $\llbracket f \rrbracket = f^+ - f^-$ is the difference of the enclosed quantity between the forward and rearward sides. Using the coordinate transformation (2.8) this reduces to

$$\frac{d\psi}{d\hat{x}} = \phi^+ + \phi^- - 1. \quad (2.15)$$

For the shock in question, the concentration ϕ^- within the expansion fan is given by (2.11) and $\phi^+ = 0$. The jump condition (2.15) therefore yields the ordinary differential equation

$$\frac{d\psi}{d\hat{x}} = \frac{1}{2} \left(\frac{\psi - \psi_r}{\hat{x} - \hat{x}_A} - 1 \right), \quad (2.16)$$

which must be solved subject to the boundary condition that the shock starts at $(\hat{x}_B, 0)$ in mapped coordinates. Using (2.13) it follows that the shock is given by

$$\psi = \psi_r - (\hat{x} - \hat{x}_A) + 2\sqrt{-\psi_r} \sqrt{\hat{x} - \hat{x}_A}, \quad (2.17)$$

where the constant $\sqrt{-\psi_r}$ is real. The shock propagates downwards, reaching $\psi = \psi_r$ at

$$\hat{x}_C = \hat{x}_A - 4\psi_r, \quad (2.18)$$

which marks the furthest downstream position of the lens. Below $\psi = \psi_r$ the flow direction, and hence the time-like direction for the characteristic curves, reverses. Theorem 3.1 of Shearer *et al.* (2008) implies that previously stable inversely graded shock structure above $\psi = \psi_r$ becomes unstable below this line. Instead a rarefaction is formed at (\hat{x}_C, ψ_r) and the concentration within the fan is given by

$$\phi = \frac{1}{2} \left[1 + \frac{\psi - \psi_r}{\hat{x} - \hat{x}_C} \right]. \quad (2.19)$$

Note that along $\psi = \psi_r$ the concentration in the upper (2.11) and lower (2.19) expansions is equal to 1/2, so they fit together without a jump in concentration. In the lower expansion the characteristic curves propagate downwards into the material fed in from the right-hand side below the $\psi = \psi_r$ line and the concentration ranges from [0, 1/2]. The $\phi = 0$ characteristic

$$\psi = \psi_r + \hat{x}_C - \hat{x} \quad (2.20)$$

marks the boundary of the lens and the large-particle region. It intersects with the downstream section of the sharp concentration shock at height $\psi = 0$ and position

$$\hat{x}_D = \hat{x}_C + \psi_r. \quad (2.21)$$

Since there are no more large particles being fed in from the right, nor any being squeezed up from below, the small particles separate out into a pure phase across a concentration shock that starts at $(\hat{x}_D, 0)$ in mapped coordinates. Ahead of the shock $\phi^+ = 1$ and behind the shock ϕ^- is given by (2.19). The shock condition (2.15) therefore yields a linear ordinary differential equation for the shock position, with solution

$$\psi = \psi_r - (\hat{x}_C - \hat{x}) + 2\sqrt{-\psi_r} \sqrt{\hat{x}_C - \hat{x}}. \quad (2.22)$$

This reaches the zero mean flow line, $\psi = \psi_r$, at

$$\hat{x} = \hat{x}_C + 4\psi_r = \hat{x}_A, \quad (2.23)$$

which is the same position \hat{x}_A as the start of the upper expansion fan. The Lax entropy condition (Shearer *et al.* 2008) predicts that a continuation of the lower

shock is unstable. It is therefore replaced by an expansion fan centred at (\hat{x}_A, \hat{z}_r) , justifying our original assumption (2.11). The lens structure is now complete. It consists of two shocks, (2.17) and (2.22), and two expansion fans, (2.11) and (2.19), that are arranged in a ‘lens’-like structure that propagates downstream with speed u_{lens} given by (2.2). In transformed mapped coordinates this solution has 180° rotational symmetry about its centre if ϕ is also mapped to $1 - \phi$.

The advantage of the transformation (2.3) and the mapping (2.8) is that this solution is universal. It is valid for uniform-thickness flows with arbitrary monotonically increasing downslope velocity profile $u(z)$, constant segregation number S_r , and constant upstream and downstream shock heights H_{up} and H_{down} . Specific cases are shown in figure 4. The first three sets of solutions have a linear velocity profile with basal slip

$$u = \alpha + 2(1 - \alpha)z, \quad 0 \leq \alpha < 1. \quad (2.24)$$

The case $\alpha = 0$ corresponds to simple shear and as α is increased towards unity the velocity shear becomes progressively less and the surface velocity and basal slip velocity become closer to one another. Formally we exclude the case of plug flow, when $\alpha = 1$, as the inversely graded concentration shock does not steepen and break. Equation (2.2) implies that the lens propagates downstream with speed

$$u_{lens} = \alpha + (1 - \alpha)(H_{up} + H_{down}). \quad (2.25)$$

In the moving transformed frame equations (2.3) and (2.5) imply the relative downstream velocity

$$\hat{u} = (1 - \alpha)(H_{up} - H_{down})(2\hat{z} - 1), \quad (2.26)$$

which is zero at $\hat{z}_r = 1/2$. In untransformed variables $z_r = (H_{up} + H_{down})/2$ lies halfway between the upper and lower shocks. The flux coordinate mapping (2.8) implies that for the linear velocity field the ψ and \hat{z} coordinates are related by the quadratic

$$\psi = (1 - \alpha)(H_{up} - H_{down})(\hat{z}^2 - \hat{z}), \quad (2.27)$$

and $\psi_r = -(1 - \alpha)(H_{up} - H_{down})/4$. The solution can now be mapped back from (2.11), (2.17), (2.19) and (2.22) by solving the quadratic (2.27) for \hat{z} and then rescaling using (2.3). For the linear velocity profiles (2.24) the lens width (2.18) at arbitrary time t in untransformed-unmapped coordinates becomes

$$x_C - x_A = \frac{1}{S_r}(1 - \alpha)(H_{up} - H_{down})^2. \quad (2.28)$$

Results for three different sets of parameters are shown in figure 4(a–c). A contour scale is used for the concentration ϕ , with darker regions corresponding to higher concentrations of large particles and lighter regions to higher concentrations of fines. The lens connects the upstream and downstream sections of the constant-height inversely graded concentration shock. The problems have all been scaled so that the depth-integrated downslope velocity is equal to unity. In the first two problems $H_{up} = 0.9$, $H_{down} = 0.1$ and (2.25) implies that u_{lens} is also equal to unity. The width of the lens is proportional to the shear rate $1 - \alpha$, inversely proportional to the segregation number S_r and proportional to the lens height squared, by equation (2.28), i.e. stronger segregation makes the lens smaller, while higher shear and larger upstream to downstream shock height differences increase its size. As the shear in figure 4(a) is twice that in figure 4(b) the lens is twice the width for the same S_r . In general, however, increased shear tends to increase the segregation rate, S_r , so these two effects may cancel out in practical situations. In figure 4(c) the velocity field is

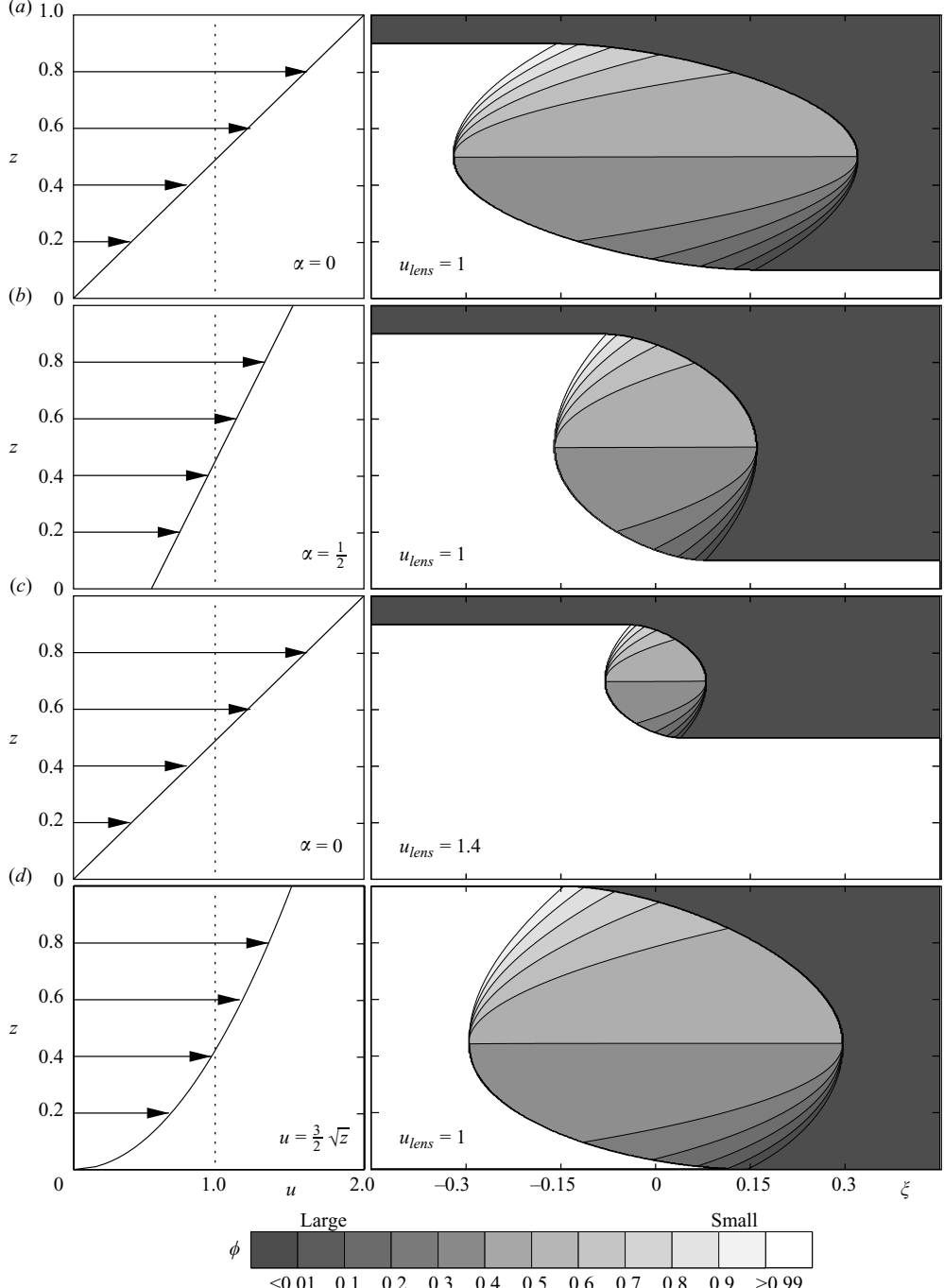


FIGURE 4. Travelling wave solutions for the concentration of small particles ϕ as a function of the downslope coordinate $\xi = x - u_{lens}t$ and the avalanche depth z . The contour scale is lighter for regions with higher concentrations of fines. In all the plots the concentration of coarse particles equals $1 - \phi$, the segregation number $S_r = 1$ and the downstream velocity profile is shown on the left. For the linear velocity profiles the parameters are (a) $\alpha = 0$, $H_{up} = 0.9$, $H_{down} = 0.1$, (b) $\alpha = 1/2$, $H_{up} = 0.9$, $H_{down} = 0.1$, and (c) $\alpha = 0$, $H_{up} = 0.9$, $H_{down} = 0.5$. (d) A nonlinear velocity profile with $H_{up} = 1$ and $H_{down} = 0$. In each case the depth-integrated velocity of the flow is normalized to unity and the downstream lens speed u_{lens} is indicated. The scaling of the lens is discussed in (2.28).

exactly the same as in figure 4(a), but $H_{up} = 0.9$ and $H_{down} = 0.5$. The lens therefore propagates faster than the mean flow, with speed $u_{lens} = 1.4$, and, while it is half the height of the first case, it is only a quarter of the width. The lens does not scale proportionally, because the velocity difference between the top and bottom of the lens also scales with the lens height, producing the quadratic dependence in (2.28).

Figure 4(d) shows the solution for a nonlinear parabolic downstream velocity profile given by

$$u = \frac{3}{2}\sqrt{z}, \quad (2.29)$$

with $H_{up} = 1.0$, $H_{down} = 0$ and $S_r = 1.0$. The lens speed is equal to unity and $\hat{u} = 3\sqrt{z}/2 - 1$. It follows that the no-mean-flow line $z_r = 4/9$ ($\psi_r = -4/27$) lies just below the mid-point due to the asymmetry in the velocity field. The upper expansion is therefore slightly larger than the lower one, reflecting the fact that there is a greater relative mass flux in the lower layers of the flow. Although this lens extends through the entire depth of the avalanche, it is actually slightly narrower than the linear case shown in figure 4(a).

3. Particle recirculation

The most important consequence of breaking size segregation waves is the fact that they allow particles to recirculate in the flow. Evidence for recirculation zones comes from both geological field observations (Pierson 1986; Vallance 2000; Iverson & Vallance 2001; Iverson 2005) and small-scale experiments with particles of different sizes and roughnesses (Pouliquen *et al.* 1997; Pouliquen & Vallance 1999). We now investigate this further by reconstructing the particle paths of the large and small particles as they travel through the lens. For each constituent the particle paths are given by

$$\frac{dx^\mu}{dt} = u^\mu, \quad \frac{dz^\mu}{dt} = w^\mu, \quad (3.1)$$

where the superscripts $\mu = l, s$ indicate variables associated with the large or small particles, respectively. Gray & Thornton (2005) and Thornton *et al.* (2006) showed that to leading order the constituent velocities normal and parallel to the chute are

$$u^s = u, \quad w^s = w - S_r(1 - \phi), \quad u^l = u, \quad w^l = w + S_r\phi. \quad (3.2)$$

Using the assumed velocity field (2.1) and the transformation of variables (2.3) it follows from (3.1) and (3.2) that the non-dimensional equations for the particle trajectories in the moving-coordinate system are

$$\frac{d\hat{x}^s}{d\hat{t}} = \hat{u}, \quad \frac{d\hat{z}^s}{d\hat{t}} = -(1 - \phi), \quad \frac{d\hat{x}^l}{d\hat{t}} = \hat{u}, \quad \frac{d\hat{z}^l}{d\hat{t}} = \phi. \quad (3.3)$$

Eliminating \hat{t} and using the coordinate mapping (2.8) implies that the small- and large-particle paths satisfy the parameter-independent equations

$$\frac{d\psi^s}{d\hat{x}^s} = -(1 - \phi), \quad \frac{d\psi^l}{d\hat{x}^l} = \phi. \quad (3.4)$$

The particle paths can therefore be reconstructed from our knowledge of the small-particle concentration in the lens-like solutions derived in § 2.

3.1. Small-particle paths

Let us follow the trajectory of small particles as they enter from the left-hand side at height $z_{enter}^s > z_r$. This is equivalent to height ψ_{enter}^s in transformed-mapped

coordinates. In the 100 % fines region $\phi = 1$ and the differential equation (3.4) has the trivial solution that the particles move to the right at constant height, ψ_{enter}^s , until they cross the outermost characteristic (2.12) of the lens at

$$\hat{x}_{\text{enter}}^s = \hat{x}_A + \psi_{\text{enter}}^s - \psi_r. \quad (3.5)$$

Once inside the upper expansion fan the concentration is given by (2.11) and (3.4) reduces to a linear ordinary differential equation. Using (3.5) this can be solved subject to the boundary condition that the particles enter at $(\hat{x}_{\text{enter}}^s, \psi_{\text{enter}}^s)$ to give the trajectory

$$\psi^s = \psi_r - (\hat{x}^s - \hat{x}_A) + 2\sqrt{\psi_{\text{enter}}^s - \psi_r} \sqrt{\hat{x}^s - \hat{x}_A}. \quad (3.6)$$

This crosses the $\psi = \psi_r$ line at

$$\hat{x}_{\text{cross}}^s = \hat{x}_A + 4(\psi_{\text{enter}}^s - \psi_r) \quad (3.7)$$

and continues into the lower expansion. Here the concentration is given by (2.19) and the trajectory (3.4) is also determined by a linear ordinary differential equation. Noting that the time-like direction is reversed this can be solved subject to the boundary condition that the particles flow into the lower fan at $(\hat{x}_{\text{cross}}^s, \psi_r)$. Using (2.18) and (3.7) this implies that the trajectory through the lower fan is

$$\psi^s = \psi_r + (\hat{x}_C - \hat{x}^s) - 2\sqrt{-\psi_{\text{enter}}^s} \sqrt{\hat{x}_C - \hat{x}^s}. \quad (3.8)$$

Finally, the small particles cross the lower shock (2.22) at

$$\hat{x}_{\text{exit}}^s = \hat{x}_C - (\sqrt{-\psi_r} + \sqrt{-\psi_{\text{enter}}^s})^2, \quad \psi_{\text{exit}}^s = \psi_{\text{enter}}^s, \quad (3.9)$$

and propagate to the right away from the lens at constant height ψ_{exit}^s in the upper domain. The small-particle paths are therefore determined by equations (3.5), (3.6), (3.8) and (3.9), and are parameterized by the mapped inflow height ψ_{enter}^s .

3.2. Large-particle paths

The large-particle paths can be constructed in a similar fashion. They enter from the bottom right-hand side at a height $z_{\text{enter}}^l \leq z_r$, which in transformed-mapped coordinates corresponds to ψ_{enter}^l . At this height the large particles are moving downslope slower than the lens. Thus, relative to the lens, the large particles move back at constant height through the region of pure coarse grains until they intersect with the lead characteristic (2.20) at

$$\hat{x}_{\text{enter}}^l = \hat{x}_C + \psi_r - \psi_{\text{enter}}^l. \quad (3.10)$$

Once inside the lens a linear ordinary differential equation for the particle path can be constructed by substituting the lower fan concentration (2.19) into (3.4). Solving subject to the condition that the particle first enters the lens at $(\hat{x}_{\text{enter}}^l, \psi_{\text{enter}}^l)$ and using (3.10) yields the path

$$\psi^l = \psi_r - (\hat{x}_C - \hat{x}^l) + 2\sqrt{\psi_{\text{enter}}^l - \psi_r} \sqrt{\hat{x}_C - \hat{x}^l}. \quad (3.11)$$

The large particles continue to move to the left as they rise up through the expansion fan and reach the zero mean velocity line, $\psi = \psi_r$, at

$$\hat{x}_{\text{cross}}^l = \hat{x}_C + 4(\psi_r - \psi_{\text{enter}}^l), \quad (3.12)$$

where they cross into the upper expansion fan (2.11). The large-particles are now swept downstream relative to the lens and continue to rise. Solving (3.4) subject to

the initial condition $(\hat{x}_{cross}^l, \psi_r)$ and using (2.18) and (3.12) to simplify the result, yields the trajectory

$$\psi^l = \psi_r + (\hat{x}^l - \hat{x}_A) - 2\sqrt{-\psi_{enter}^l} \sqrt{\hat{x}^l - \hat{x}_A}. \quad (3.13)$$

The large particles finally exit the lens when they cross the upper shock (2.17) at

$$\hat{x}_{exit}^l = \hat{x}_A + (\sqrt{-\psi_r} + \sqrt{-\psi_{enter}^l})^2, \quad \psi_{exit}^l = \psi_{enter}^l, \quad (3.14)$$

and move at constant height downstream. The large-particle paths are given by equations (3.10), (3.11), (3.13) and (3.14), and are parameterized by ψ_{enter}^l . The expressions for the large-particles paths are closely analogous to the ones for the small grains. In fact, the results are identical (in transformed-mapped variables) under a 180° rotation about the centre of the lens.

3.3. Combined structure

The particle paths can be mapped from transformed-mapped coordinates (\hat{x}, ψ) to our original non-dimensional coordinates (x, z) , at an arbitrary time t , by constructing the inverse mapping to (2.8) and reversing the transformation (2.3). The results for the four travelling wave solutions derived in § 2 are shown in figure 5. Large particles that lie below the $z=z_r$ line propagate downslope slower than the lens and are eventually caught up by it. Relative to the lens, they appear to propagate at constant height backwards until they enter the lens and are pushed upwards by squeeze expulsion. In the lower expansion fan the particles start off from the horizontal trajectory and curve upwards with increasing slope, until they cross the no-mean-flow line $z=z_r$ with an infinite gradient. The key reason for this is that the mapping (2.8) implies that $dz/dx = (1/\hat{u}) d\psi/dx$, so in the limit as $z \rightarrow z_r$ and $\hat{u} \rightarrow 0$ the gradient $dz/dx \rightarrow \infty$. Once the large particle crosses into the upper fan it is swept to the right as it continues to rise. It eventually hits the upper-right concentration shock and moves downslope relative to the lens along a constant-height trajectory between $z=z_r$ and $z=H_{up}$. Large particles that enter at the lowest and slowest levels are therefore recirculated back onto the downstream side at the highest and fastest levels. Interestingly the lowest large-particle path, which enters at $\psi_{enter}^l=0$ and is given by (3.11) and (3.13), is identical to the lower shock (2.22) and the lead expansion (2.12). In figure 5(a–c) there are also some large particles that lie above $z=H_{up}$, that enter from the left and stay on a constant-height trajectory until they exit on the right.

Small particles enter from the left between $z=z_r$ and $z=H_{up}$, cross the lead characteristic (2.12) and percolate down through the lens by kinetic sieving. They start by propagating downwards and to the right, but, as they cross the no-mean-flow line with infinite gradient, they are swept back to the left. They exit the lens as they cross the lower concentration shock (2.22) and are recirculated backwards at constant height in the region $[H_{down}, z_r]$. This time the highest small-particle path $\psi_{enter}^s=0$ has a trajectory given by (3.6) and (3.8), that exactly corresponds to the upper concentration shock (2.17) and the lower lead expansion (2.20). The correspondence of the large- and small-particle paths with the boundaries of the lens helps to explain why it appears to be skewed to the left. Small particles percolate downwards at a speed that is proportional to the concentration of large particles. Since there are higher concentrations of large particles lower down in the lens, the small particles accelerate as they descend. The downward trajectory in the upper expansion is therefore much longer than in the lower fan. Conversely, large particles are squeezed up faster where there are higher concentrations of fines. They therefore propagate upwards faster

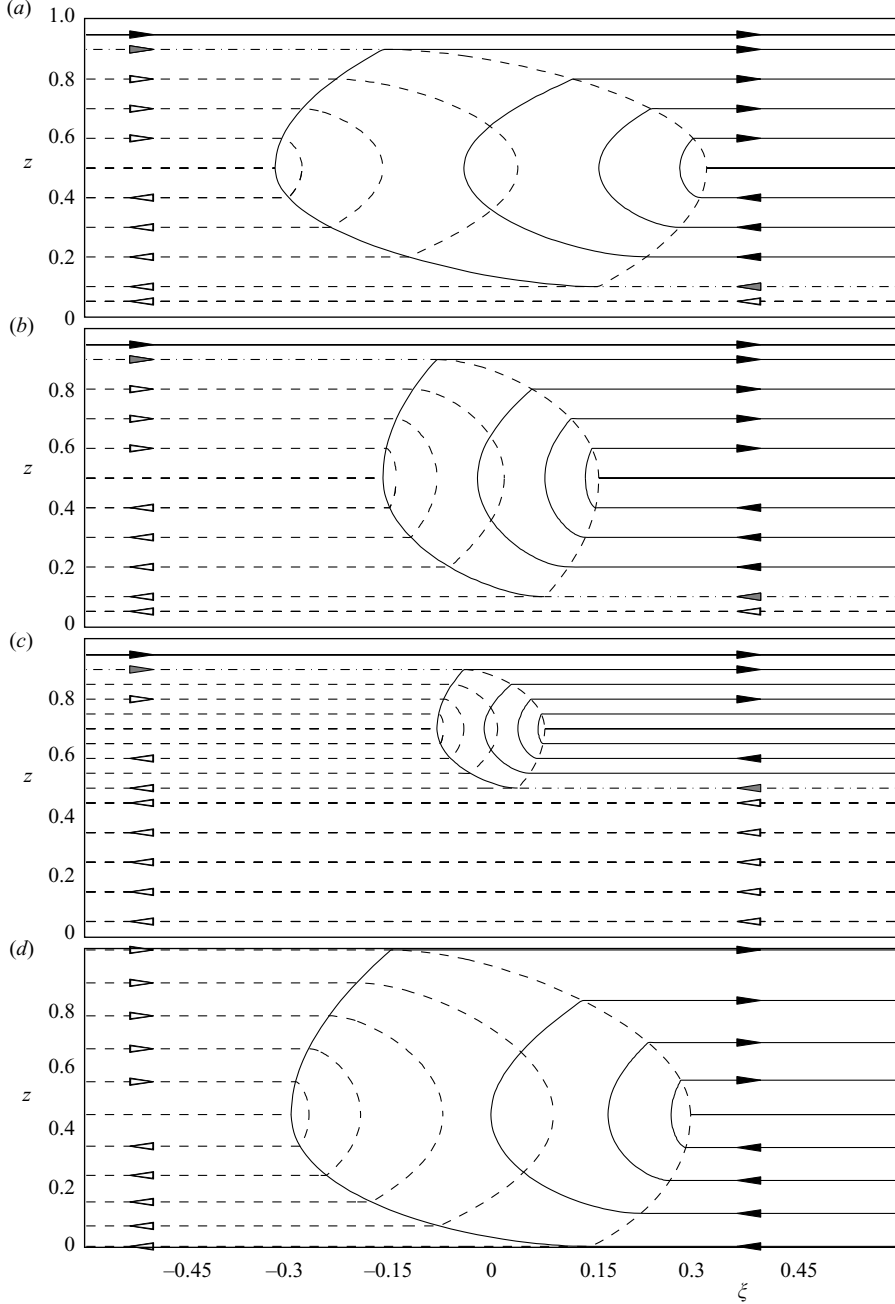


FIGURE 5. The particle paths for the same cases as shown in figure 4. The large-particle paths are shown using a solid line with a black arrow and the small-particle paths are shown using dashed lines and a white arrow. The upstream and downstream shocks are shown with dot-dash lines and grey arrows to indicate that both large and small particles propagate on either side of the line. The intersection of the highest small-particle path and lowest large-particle path delineates the boundary of the lens. Recirculation of the particles occurs between H_{up} and H_{down} . Small particles enter from the top left above z_r , percolate down through the lens and are ejected on the bottom left side, while large particles propagate in from the bottom right, rise through the lens and exit on the top right.

the higher they are. These effects are strongest for the bounding particle paths and become less strong the closer the particles are to $z = z_r$ as they enter. Small particles may also enter from the right below H_{down} and move at constant height to the left without entering the lens. Figure 5(c) has a large region of such small particles.

Figure 5(d) shows the solution for the nonlinear velocity profile (2.29). The particle paths are similar to the linear velocity cases, except that they are skewed into the lower half of the plot, reflecting the higher relative mass flux in the lower regions. All the particle paths have infinite gradient as they cross the no-mean-flow line at $z_r = 4/9$. Note that although there is no exact inverse mapping to (2.8) for the velocity field (2.29), exact solutions can still be constructed by graphing along the z -axis rather than the x -axis.

4. Temporal behaviour of the lens

Unlike classical breaking waves (e.g. Lighthill 1978; Stoker 1957) the steady-state lens does not develop immediately after breaking. We investigate the temporal behaviour using a shock-capturing numerical method, described by Gray & Thornton (2005), to solve the problem in an unstretched coordinate system translating downslope with the speed of the lens. For a steady uniform flow (2.1) in simple shear ($\alpha = 0$) the non-dimensional segregation equation becomes

$$\frac{\partial \phi}{\partial t} + \frac{\partial}{\partial \xi}(\phi \hat{u}) - \frac{\partial}{\partial z}(S_r \phi(1 - \phi)) = 0, \quad (4.1)$$

where the translating coordinate ξ and the relative velocity \hat{u} are

$$\xi = x - u_{lens}t, \quad \hat{u} = 2z - 1. \quad (4.2)$$

This assumes that the speed of the lens u_{lens} is equal to unity and the no-mean-flow line $z_r = 1/2$. A necessary condition for a steady state to develop with $u_{lens} = 1$ is that the upstream and downstream inversely graded shock heights H_{up} and H_{down} sum to unity, by (2.25). We focus on the case $S_r = 1$ and inflow conditions

$$H_{up} = 0.9, \quad H_{down} = 0.1, \quad (4.3)$$

which corresponds to the first steady-state problem in figure 4(a). Note that since the relative flow direction changes across $z = z_r$, we must allow outflow conditions along $[z_r, 1]$ on the right, and $[0, z_r]$ on the left, of the domain. The domain must also be sufficiently large for the lens to develop without crossing the boundaries. At the free surface and base of the flow we impose the condition of no normal particle flux

$$\phi(1 - \phi) = 0, \quad z = 0, 1. \quad (4.4)$$

The numerical method is based on a simple TVD Lax Friedrichs scheme (Yee 1989; Toth & Odstrcil 1996) and uses Godunov-type operator splitting (e.g. LeVeque 2002). It has been extensively tested against both steady-state and fully time-dependent exact solutions (Gray & Thornton 2005; Thornton *et al.* 2006; Gray *et al.* 2006; Shearer *et al.* 2008) with evolving shocks and expansion fans. All the computations are performed on a rectangular domain $[-1.5, 1.5] \times [0, 1]$ at grid resolutions ranging from 100×100 to 1500×1500 , with a superbee slope limiter and a CFL number equal to $1/2$.

The initial condition is shown in figure 6(a). The inversely graded concentration shock has a linearly decreasing section between $\xi = -0.8$ and $\xi = 0.8$, which joins two sections at constant heights H_{up} and H_{down} . For the far-field conditions (4.3) the

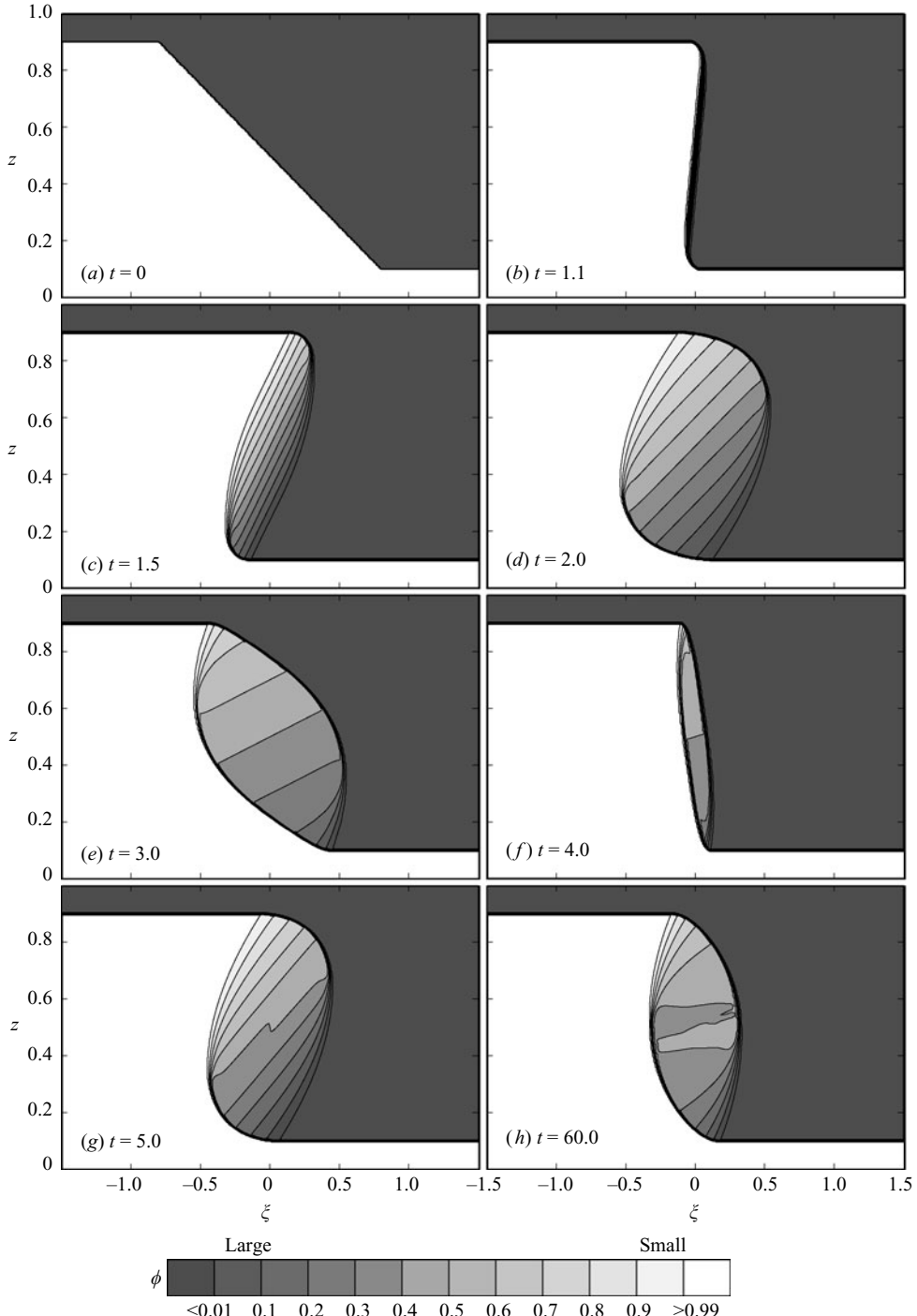


FIGURE 6. A series of contour plots showing the development of the small-particle concentration in a temporally evolving lens in a frame (ξ, z) moving at the same speed as the steady-state lens $u_{\text{lens}} = 1$. The initial condition is shown in (a) and the monotonically decreasing section of the initial concentration shock breaks at $t = 1$. The results are for linear shear $\hat{u} = 2z - 1$ and $S_r = 1$, which correspond to the steady-state solution in figure 4(a). Computations are performed on a 300×300 grid and an animation of the solution is available with the online version of the paper.

equation of the line is $x = -(2z - 1)$. It is a simple matter to show that, for the relative velocity field given by (4.2), the line steepens and breaks simultaneously along $x = 0$ at time $t = 1$. The behaviour shortly after the solution has broken is shown at $t = 1.1, 1.5, 2.0$ and 3.0 in figure 6(b–e). The vertical shock breaks into an expansion fan that initially lies along $x = 0$. As time increases the fan rapidly spreads out and is tilted to the right in response to the velocity shear. In order to close the ends of this fan, concentration shocks are initiated from both the top and bottom of the lens and these break into two secondary expansions at the points where the concentration shock gradients become infinite. The width of the transient lens at $t = 2\text{--}3$ non-dimensional time units is approximately equal to unity, which is nearly twice as wide as the steady-state solution shown in figure 4. The upper secondary expansion propagates downwards, while the lower secondary expansion propagates upwards. They appear to reach the opposite side at approximately $t = 4$ when the transient lens almost completely closes up and the process appears to repeat itself.

The solution continues to oscillate, precessing like a spinning ‘rugby’ ball between an expanded and contracted state with a period of approximately four non-dimensional time units. The amplitude of the oscillations decays with increasing time and the initial expansion region becomes smaller and smaller until the solution is very close to the steady-state solution shown in figure 4(a) by time $t = 60$. The only significant deviation from the exact solution is the 50 % contour, which should lie at $z = 0.5$, but instead looks rather wavy. This is an artifact of the TVDLF scheme and stems from the fact that the local wave speed $(2\phi - 1)$ is zero, which implies that some accuracy is lost. Local concentration errors are still less than 3 %, but the deviations of the 50 % contour are accentuated because gradients in ϕ are very small at the centre of the lens. Despite its complicated dynamics the lens settles down at the centre of the domain, confirming that it propagates downslope with speed unity. An animation of the time-dependent lens is available with the online version of the paper.

Grid-independence tests have been performed to confirm that the solution does relax towards the steady state. The mean absolute difference \mathcal{E} between the computed solution ϕ_{ij} and the steady-state solution ϕ_{ij}^\dagger at the centre of each grid cell (i, j) is used as a measure:

$$\mathcal{E} = \frac{1}{n^2} \sum_{ij} |\phi_{ij} - \phi_{ij}^\dagger|, \quad (4.5)$$

where n are the number of points in both the ξ - and z -directions, respectively. A semi-log plot of \mathcal{E} with increasing time is shown in figure 7 for three different grid resolutions. There is a small initial transient, shown in the inset panel, prior to breaking at $t = 1$. However, for long time the time-dependent solution decays exponentially towards the steady state. This is shown by the dashed line in figure 7, which implies that

$$\mathcal{E} \approx \exp(-t/18), \quad (4.6)$$

and the decay is therefore quite slow as the inflow and outflow equilibrate. This holds for all grid resolutions, demonstrating that the numerical solutions are well resolved. The numerical solution eventually departs from this behaviour at a time that is resolution dependent. The change in behaviour is caused by the solution being within numerical error of the steady state. From an analysis of the straight line segments on figure 7 we can deduce that the error in capturing the steady-state solutions is proportional to $1/n$, i.e. doubling the number of points in each direction halves the error. Closer inspection shows that small oscillations develop as the solution begins

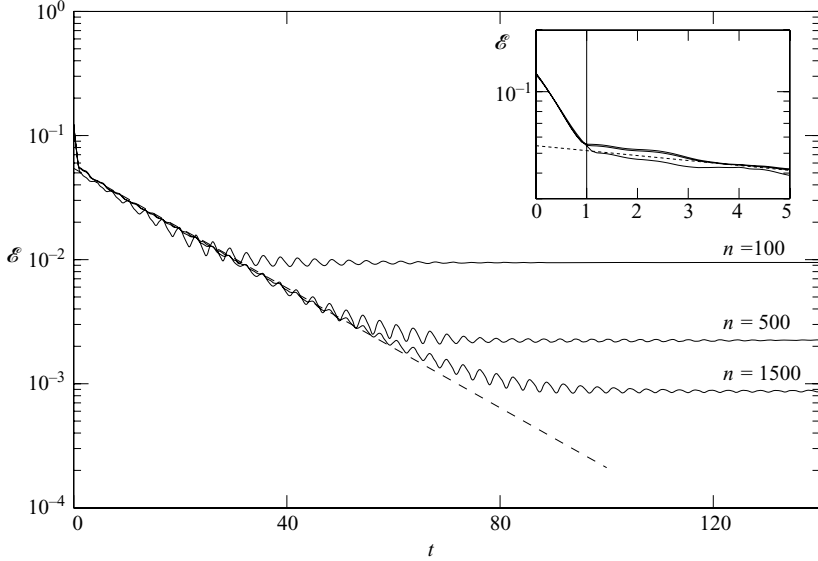


FIGURE 7. The evolution of the global absolute difference \mathcal{E} between the numerical breaking wave solution and the exact steady-state solution on a semi-log plot for three different grid resolutions with $n \times n$ points. The dashed line shows that the solution decays exponentially for large time. The inset panel shows the early time behaviour.

to depart from the exponentially decaying behaviour. This is caused by the method ‘over-shooting’ the exact solution. The decay of these oscillations is due to the artificial diffusion inherent in the scheme, which is less at higher resolutions.

5. Lens interaction

We now consider a more complicated situation in which two lenses at different heights and with different downslope velocities interact and merge. The initial configuration is shown in figure 8(a). It consists of three slope-parallel concentration shocks at heights $H_{up} = 0.9$, $z_r = 0.5$ and $H_{down} = 0.1$ that are joined by sharp steps at $\xi = -1.3$ and $\xi = 1.3$. Each of the two vertical sections breaks at $t = 0$ and two lenses form that are both similar to the previous breaking wave problem, i.e. spinning like a rugby ball, and opening and closing up as they propagate downstream. The upper lens is located between z_r and H_{up} , and propagates downstream with a speed of 1.4 non-dimensional units. The lower shock is in the slower part of the flow between H_{down} and z_r , and propagates downstream with a speed of 0.6 non-dimensional units. The solutions are computed in a frame moving downslope with speed unity. It therefore appears that the upper lens moves to the right, while the lower lens moves to the left at the same speed of 0.4 non-dimensional units. These are both consistent with the speed of propagation of a steady-state lens implied by equations (2.2) and (2.5). The two lens are shown at times $t = 1, 2$ and 3 in figure 8(b–d). The lenses meet at 3.25 non-dimensional units and very quickly merge to form a single large precessing lens between H_{up} and H_{down} that propagates downslope with speed unity. Figure 9 shows the evolution of the global absolute difference \mathcal{E} , defined in (4.5), between the computed concentration and the exact steady-state solution. While the initial behaviour is different, after $t = 3.25$ the mean absolute difference \mathcal{E} decays exponentially for long time in exactly the same way as in equation (4.6) for the

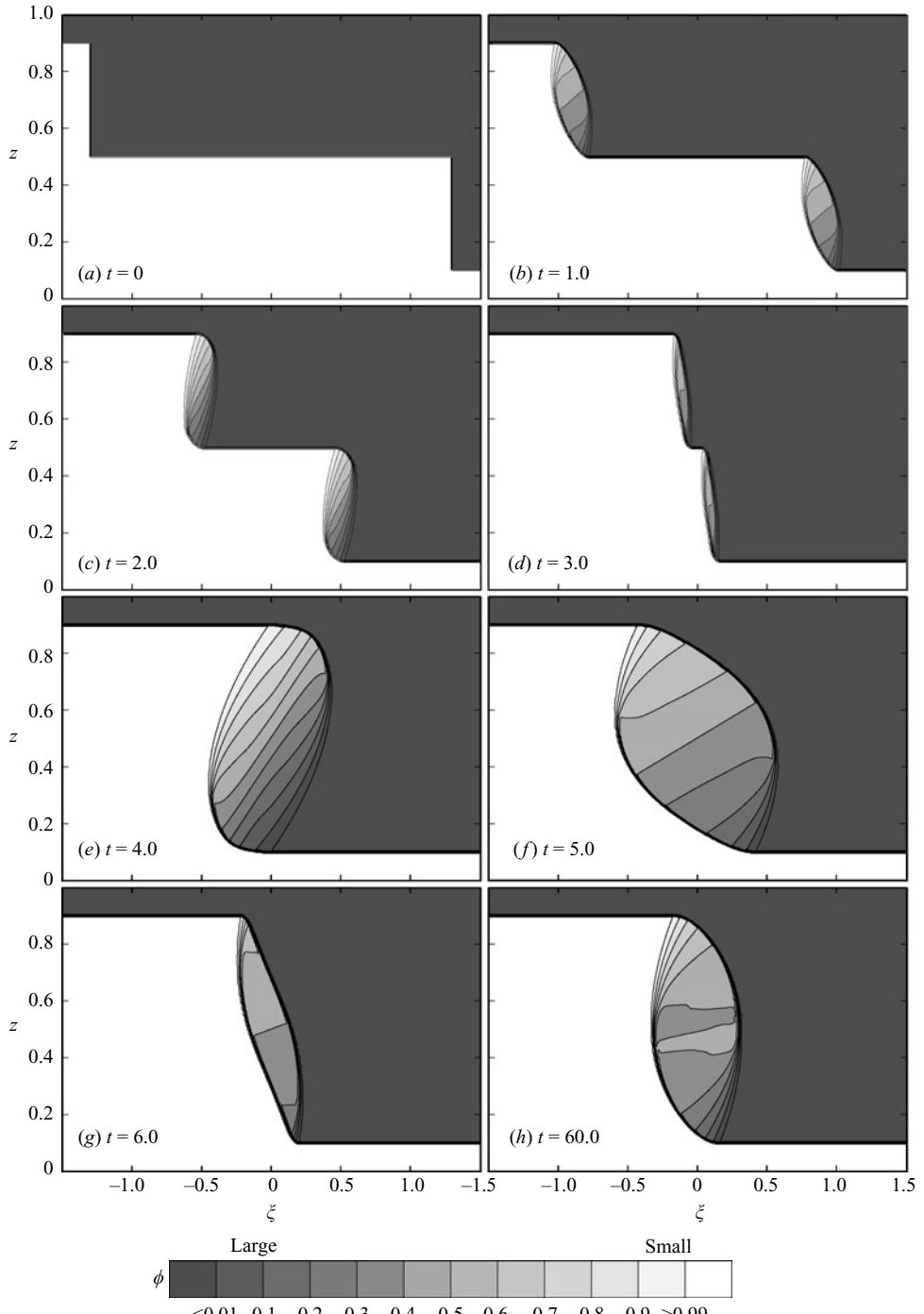


FIGURE 8. A series of contour plots showing the development of the small-particle concentration during the interaction of two breaking lenses in a frame (ξ, z) moving downslope with speed unity. The initial condition is shown in (a). At $t = 0$ the sharp downward steps in concentration break to form two lenses that propagate in opposite directions with speed 0.4. Just after $t = 3$ these begin to coalesce to form a single lens between $H_{up} = 0.9$ and $H_{down} = 0.1$ that propagates downslope with speed unity. The results are for linear shear $\hat{u} = 2z - 1$ and $S_r = 1$, which correspond to the steady-state solution in figure 4(a). Computations are performed on a 300×300 grid and an animation of the solution is available with the online version of the paper.

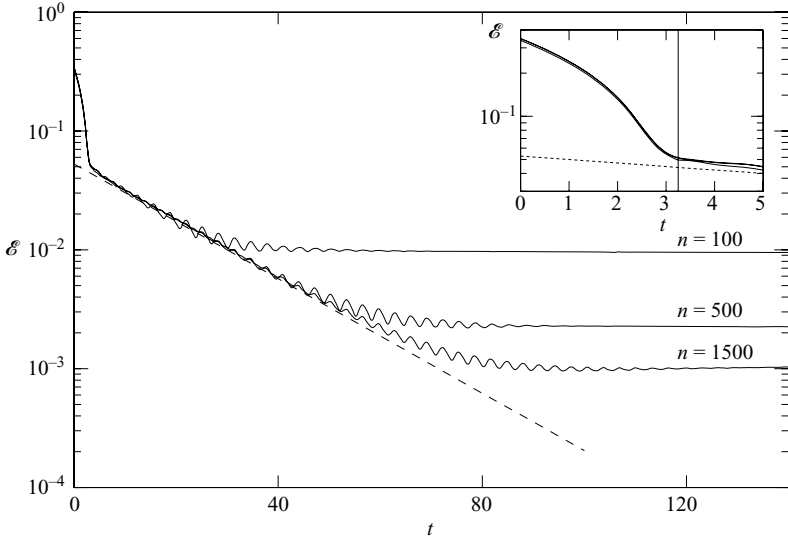


FIGURE 9. The evolution of the global absolute difference \mathcal{E} between the time-dependent lens interaction problem and the exact steady-state solution on a semi-log plot for three different grid resolutions with $n \times n$ points. The dashed line shows that the solution decays exponentially for large time. The inset panel shows the early time behaviour.

previous problem in § 4. This slow exponential decay is indicated on figure 9 by a dashed line. By $t = 60$ non-dimensional time units the solution shown in figure 8(h) is very close to the steady state shown in figure 4(a) apart from the 50 % contour. An animation of the solution is available with the online version of the paper.

It is possible to construct an infinite set of exact solutions with two or more lenses that are stacked in a series of steps starting at H_{up} and ending at H_{down} . However, velocity shear always ensures that these coalesce in finite time, as in the lens interaction problem shown in figure 8. In extensive numerical tests the solution always evolves to the single lens and this is stable to two-dimensional perturbations. This suggests that, while a single large lens is not a unique solution, it is the only stable travelling wave solution to the problem illustrated in figure 1.

6. Discussion and conclusions

Pouliquen *et al.* (1997) and Pouliquen & Vallance (1999) have observed that large particles recirculate at the front of bi-disperse granular mixtures as they flow down a slope and break into a series of fingers. They postulated that the large particles rose to the faster moving free-surface layers by kinetic sieving and were then transported to the flow front, where they were over-run, and segregated back up to the surface again to form a recirculation loop. In this paper we have used a hyperbolic segregation theory, that stems from the work of Savage & Lun (1988), Gray & Thornton (2005) and Thornton *et al.* (2006), to derive an exact travelling wave solution for the small-particle concentration within the recirculation zone as well as the particle paths of each species. The solution consists of two concentration expansions and two concentration shocks that form a ‘lens’-like structure that propagates downslope at the average speed of the layer. Within the lens the small particles percolate down by kinetic sieving and the large ones rise-up by squeeze expulsion until they separate out

into pure phases across the concentration shock. The large particles are recirculated on the downstream side of the lens, exactly as postulated by Pouliquen *et al.* (1997) and Pouliquen & Vallance (1999). Breaking size segregation waves in which the particles are recirculated are a generic feature of hyperbolic segregation theories. They develop whenever a monotonically decreasing section of concentration between pure phases is sheared and breaks, as in the solutions of Gray *et al.* (2006).

A shock-capturing TVDLF numerical method (Gray & Thornton 2005) was used to investigate the temporal evolution towards the travelling-wave solution. In the first case the shock breaks along a line and then oscillates backwards and forwards like a spinning rugby ball, opening and closing up as it converges exponentially on the exact solution. A more complex initial configuration allowed two lenses to form at different heights in the flow and with different downstream velocities. After a short time they coalesced to form a single lens that propagated downstream with the mean velocity of the layer. The behaviour of the merged lens is similar to that of the first problem, eventually decaying exponentially towards the exact solution. The decay rate of 1/18 is the same in both problems, which implies that the steady state is only approached for very long times. Animations of both solutions are available online.

Particle-size segregation models can be coupled to existing granular avalanche and geophysical mass flow models (e.g. Eglit 1983; Savage & Hutter 1989; Gray, Wieland & Hutter 1999; Wieland, Gray & Hutter 1999; Iverson & Denlinger 2001; Pouliquen & Forterre 2002; Gray, Tai & Noelle 2003; Denlinger & Iverson 2004; Mangeney-Castelnau *et al.* 2005; Patra *et al.* 2005; Gray & Cui 2007) instead of prescribing the bulk velocity $\mathbf{u}(x, y, z)$ as in this paper. All of these models use depth-integrated equations to compute the flow thickness $h(x, y)$ and the depth-averaged velocity $\bar{\mathbf{u}}(x, y)$. Using bulk incompressibility and assumed bulk velocity profiles through the avalanche depth, the velocity components (u, v, w) can be reconstructed and the small-particle concentration can then be computed using (1.1). Feedback may be introduced by coupling the basal friction and/or the bulk velocity profiles to the local concentration ϕ . Such models should be sufficient to capture the particle mobility differences that give rise to frontal instabilities, fingering and enhanced run-out in small-scale experiments (Pouliquen *et al.* 1997; Pouliquen & Vallance 1999; Phillips *et al.* 2006). In geophysical mass flows, such as debris and pyroclastic flows, the basal resistance is coupled to the pore pressure (Iverson 1997), which, in turn, is dissipated much more rapidly in regions with high concentrations of coarse particles. The bouldery margins therefore tend to be less mobile than the finer grained interior, which can again lead to instabilities. The future development of fully coupled models should lead to a fuller understanding of the spontaneous formation of coarse-grained lateral levees and distal lobes (Pierson 1986; Vallance & Savage 2000; Vallance 2000; Iverson & Vallance 2001; Iverson 2005), which are important generic features of many geological deposits.

This research was generously supported by the Natural Environment Research Council (NE/E003206/1 and NERIAS/2003/00439) and an Engineering and Physical Sciences Research Council Advanced Research Fellowship (GR/S50052/01 & GR/S50069/01), as well as support from the Manchester Institute for Mathematical Sciences (MIMS).

REFERENCES

- ARANSON, I. S. & TSIMRING, L. S. 2006 Pattern and collective behavior in granular media: Theoretical concepts. *Rev. Mod. Phys.* **78**, 641–692.

- BAGNOLD, R. A. 1954 Experiments on a gravity-free dispersion of large spheres in a newtonian fluid under shear. *Proc. R. Soc. Lond. A* **255**, 49–63.
- BRESSAN, A. 2000 *Hyperbolic Systems of Conservation Laws: The One-Dimensional Cauchy Problem*. Oxford University Press.
- BRIDGEWATER, J. 1976 Fundamental powder mixing mechanisms. *Powder Technol.* **15**, 215–236.
- COOKE, M. H., STEPHENS, D. J. & BRIDGEWATER, J. 1976 Powder mixing – a literature survey. *Powder Technol.* **15**, 1–20.
- DENLINGER, R. P. & IVERSON, R. M. 2004 Granular avalanches across irregular three-dimensional terrain: 1. theory and computation. *J. Geophys. Res.* **109** (F1), F01014.
- DOLGUNIN, V. N., KUDY, A. N. & UKOLOV, A. A. 1998 Development of the model of segregation of particles undergoing granular flow down an inclined chute. *Powder Technol.* **96**, 211–218.
- DOLGUNIN, V. N. & UKOLOV, A. A. 1995 Segregation modelling of particle rapid gravity flow. *Powder Technol.* **26**, 95–103.
- DRAHUN, J. A. & BRIDGEWATER, J. 1983 The mechanisms of free surface segregation. *Powder Technol.* **36**, 39–53.
- EGLIT, M. E. 1983 Some mathematical models of snow avalanches. In *Advances in Mechanics and the Flow of Granular Materials* (ed. M. Shahinpoor), pp. 577–588. Clausthal-Zellerfeld and Gulf Publishing Company.
- GRAY, J. M. N. T. & CHUGUNOV, V. A. 2006 Particle-size segregation and diffusive remixing in shallow granular avalanches. *J. Fluid Mech.* **569**, 365–398.
- GRAY, J. M. N. T. & CUI, X. 2007 Weak, strong and detached oblique shocks in gravity driven granular free-surface flows. *J. Fluid Mech.* **579**, 113–136.
- GRAY, J. M. N. T., SHEARER, M. & THORNTON, A. R. 2006 Time-dependent solution for particle-size segregation in shallow granular avalanches. *Proc. R. Soc. Lond. A* **462**, 947–972.
- GRAY, J. M. N. T., TAI, Y. C. & NOELLE, S. 2003 Shock waves, dead-zones and particle-free regions in rapid granular free surface flows. *J. Fluid Mech.* **491**, 161–181.
- GRAY, J. M. N. T. & THORNTON, A. R. 2005 A theory for particle size segregation in shallow granular free-surface flows. *Proc. R. Soc. Lond. A* **461**, 1447–1473.
- GRAY, J. M. N. T., WIELAND, M. & HUTTER, K. 1999 Free surface flow of cohesionless granular avalanches over complex basal topography. *Proc. R. Soc. Lond. A* **455**, 1841–1874.
- IVERSON, R. M. 1997 The physics of debris flows. *Rev. Geophys.* **35**, 245–296.
- IVERSON, R. M. 2005 Debris-flow mechanics. In *Debris Flow Hazards and Related Phenomena* (ed. M. Jakob & O. Hungr), pp. 105–134. Springer-Praxis.
- IVERSON, R. M. & DENLINGER, R. P. 2001 Flow of variably fluidized granular masses across three-dimensional terrain 1. coulomb mixture theory. *J. Geophys. Res.* **106**, 553–566.
- IVERSON, R. M. & VALLANCE, J. W. 2001 New views of granular mass flow. *Geology* **29**, 115–119.
- KHAKHAR, D. V., McCARTHY, J. J. & OTTINO, J. M. 1997 Radial segregation of granular mixtures in rotating cylinders. *Phys. Fluids* **9**, 3600–3614.
- KHAKHAR, D. V., McCARTHY, J. J. & OTTINO, J. M. 1999 Mixing and segregation of granular materials in chute flows. *Chaos* **9**, 594–610.
- KHAKHAR, D. V., ORPE, A. V. & HAJRA, S. K. 2002 Segregation of granular materials in rotating cylinders. *Physica A* **318**, 129–136.
- LEVEQUE, R. J. 2002 *Finite Volume Methods for Hyperbolic Problems*. Cambridge University Press.
- LIGHTHILL, J. 1978 *Waves in Fluids*. Cambridge University Press.
- MANGENEY-CASTELNAU, A., BOUCHUT, B., VILOTTE, J., LAJEUNESSE, E., AUBERTIN, A. & PIRULLI, M. 2005 On the use of saint-venant equations for simulating the spreading of a granular mass. *J. Geophys. Res.* **110**, B09103.
- MIDDLETON, G. V. 1970 Experimental studies related to problems of flysch sedimentation. In *Flysch Sedimentology in North America* (ed. J. Lajoie), pp. 253–272. Toronto: Business and Economics Science Ltd.
- MIDDLETON, G. V. & HAMPTON, M. 1976 Subaqueous sediment transport and deposition by sediment gravity waves. In *Marine Sediment Transport and Environmental Management* (ed. D. Stanley & D. Swift), pp. 197–218. Wiley.
- NAYLOR, M. A. 1980 The origin of inverse grading in muddy debris flow deposits – a review. *J. Sedimentary Petrol.* **50**, 1111–1116.

- PATRA, A. K., BAUER, A. C., NICHITA, C. C., PITMAN, E. B., SHERIDAN, M. F., BURSIK, M., B., R., WEBBER, A., STINTON, A. J., NAMIKAWA, L. M. & S., R. C. 2005 Parallel adaptive numerical simulation of dry avalanches over natural terrain. *J. Volcan. Geotherm. Res.* **139**, 1–21.
- PHILLIPS, J. C., HOGG, A. J., KERSWELL, R. R. & THOMAS, N. H. 2006 Enhanced mobility of granular mixtures of fine and coarse particles. *Earth Planet. Sci. Lett.* **246**, 466–480.
- PIERSON, T. C. 1986 In *Hillslope Processes* (ed. A. D. Abrahams), pp. 269–296. Allen & Unwin.
- POULQUEN, O., DELOUR, J. & SAVAGE, S. B. 1997 Fingering in granular flows. *Nature* **386**, 816–817.
- POULQUEN, O. & FORTERRE, Y. 2002 Friction law for dense granular flows: application to the motion of a mass down a rough inclined plane. *J. Fluid Mech.* **453**, 131–151.
- POULQUEN, O. & VALLANCE, J. W. 1999 Segregation induced instabilities of granular fronts. *Chaos* **9**, 621–630.
- SALLENGER, A. H. 1979 Inverse grading and hydraulic equivalence in grain-flow deposits. *J. Sedimentary Petrol* **49**, 553–562.
- SAVAGE, S. B. & HUTTER, K. 1989 The motion of a finite mass of material down a rough incline. *J. Fluid Mech.* **199**, 177–215.
- SAVAGE, S. B. & LUN, C. K. K. 1988 Particle size segregation in inclined chute flow of dry cohesionless granular material. *J. Fluid Mech.* **189**, 311–335.
- SHEARER, M., GRAY, J. M. N. T. & THORNTON, A. R. 2008 Particle-size segregation and inverse-grading in granular avalanches. *Europ. J. Appl. Maths.* (in press).
- STOKER, J. J. 1957 *Water Waves: The Mathematical Theory with Applications, Pure and Applied Mathematics : A Series of Texts and Monographs*, vol. IV. Interscience.
- THORNTON, A. R., GRAY, J. M. N. T. & HOGG, A. J. 2006 A three phase model of segregation in shallow granular free-surface flows. *J. Fluid Mech.* **550**, 1–25.
- TOTH, G. & ODSTRCIL, D. 1996 Comparison of some flux corrected transport and total variation diminishing numerical schemes for hydrodynamic and magnetohydrodynamics problems. *J. Comput. Phys.* **128**, 82–100.
- VALLANCE, J. W. 2000 *Lahars. Encyclopedia of Volcanoes*, pp. 601–616. Academic.
- VALLANCE, J. W. & SAVAGE, S. B. 2000 Particle segregation in granular flows down chutes. In *IUTAM Symposium on Segregation in Granular Flows* (ed. A. Rosato & D. Blackmore).
- WIELAND, M., GRAY, J. M. N. T. & HUTTER, K. 1999 Channelised free surface flow of cohesionless granular avalanches in a chute with shallow lateral curvature. *J. Fluid Mech.* **392**, 73–100.
- YEE, H. C. 1989 A class of high-resolution explicit and implicit shock-capturing methods. *Tech. Rep.* TM-101088. NASA.